Inertial Oscillations on the Continental Shelf of the Gulf of Lions—Observations and Theory

C. MILLOT

Antenne du Laboratoire d'Océanographie Physique du Muséum, BP2, 83501 La Seyne, France

M. CRÉPON

Laboratoire d'Océanographie Physique du Muséum, 75231 Paris-Cedex 05, France

(Manuscript received 10 April 1980, in final form 5 January 1981)

ABSTRACT

Observations in the Gulf of Lions (northwestern Mediterranean Sea) in summer have shown that gusts of wind lasting a few days generate transient upwellings and inertial motions. Oscillations at the inertial frequency were observed in current meter data near the shore and at a frequency 10% greater in the temperature data. Vertical coherences in current meter data show a strong baroclinic mode at frequencies greater than inertial frequency. A simple one-dimensional two-layer transient model suggests that these motions are associated with two different physical processes. The first process describes the local response of the ocean to meteorological forcing, the second is associated with the propagation of long internal waves generated in the transient phase of the geostrophic adjustment process. As suggested by the model, the direction of propagation of the internal waves is computed from current and temperature data measured at one point and it is found that the shore is the source zone.

1. Introduction

From 1974 to 1978 several continental shelf dynamic experiments were conducted in the Gulf of Lions in the northwestern part of the Mediterranean Sea. Their objective was to study the upwellings occurring along the shore in summer when the Mistral and the Tramontane, strong northwest winds, blow. The low-frequency structure and the spatial variability of these upwellings have been described previously (Millot, 1979). In the present paper, we discuss motions with time scale comparable to the inertial period. The Mediterranean Sea is a suitable place to make such a study because tidal periods are absent on current and temperature records. We can observe the first stages of transient motions generated in the sea by atmospheric forcing without any bias due to numerical filtering.

Inertial currents are a quasi-permanent feature of deep-sea motions (Webster, 1968). In the American Great Lakes, Verber (1964, 1966) observed oscillating flows with a period near the inertial frequency, at all depths and in all seasons. These oscillations were measured far offshore as well as only 8 km off coast. In addition, internal waves were found throughout the lakes with thermocline displacements of the order of 10 m, and temperature variations of 12°C. Current and temperature time series of the oscillations were studied by Malone (1968) using spectral analysis techniques. He found that velocity components at different depths were highly coherent near the inertial frequency, and the thermocline oscillated vertically with about the same frequency. Currents were ~180° out of phase above and below the thermocline, and nearly in phase when measured in the same layer. Pollard (1970) and Gonella (1971) have shown that inertial currents are generated in the upper layers of the ocean by the temporal variations of the local wind. Blanton (1975), in the Great Lakes, and Hayes and Halpern (1976), along the Oregon shore, found that the presence of inertial oscillations is a common feature in the first stages of transient coastal upwellings. Ivanov and Morozov (1977) and Mortimer (1977) studied the relations between current and temperature fields in the inertial frequency band. They found that generally the coherence is small and they suggested a mechanism which is the same as Crepon's model (1969). He showed that inertial oscillations are associated with two different physical processes. The first describes the local response of the ocean to the wind stress, the second is associated with the propagation of long internal waves generated in the transient phase of the geostrophic adjustment due to the forcing (Blumen, 1972). In the present paper we explain theoretically and support with data analysis the rather complex relation between current and temperature oscillations in the inertial frequency band.

0022-3670/81/050639-19$08.75

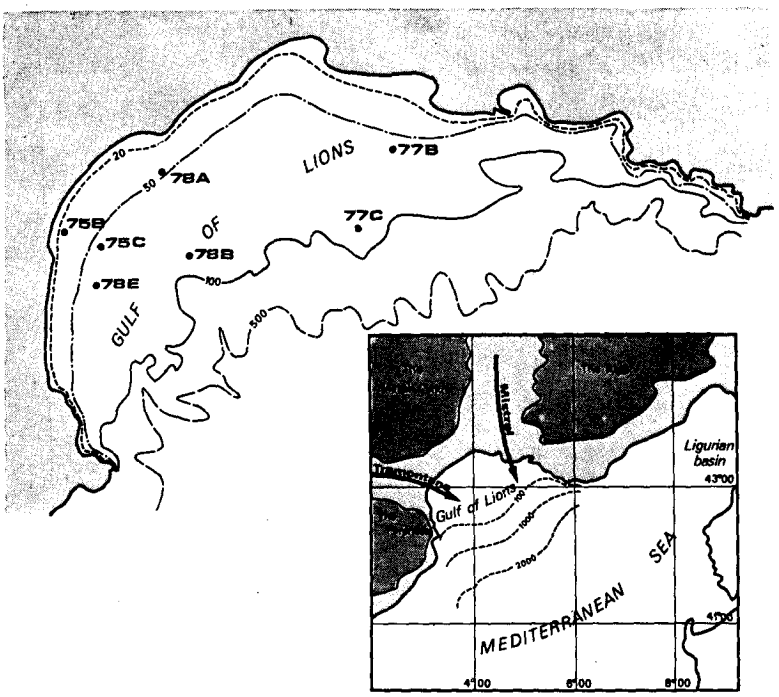

FIG. 1. Topographic features of the Gulf of Lions and position of the moorings.

The inertial motions occurring in the ocean were analyzed by Mooers (1975) in terms of three-dimensional waves. This model includes the effects of a continuous stratification and vertical shear of the horizontal current. In the Gulf of Lions, the absence of a strong mean circulation, the small depth of the continental shelf, and the presence of a well-defined mixed layer with a sharp thermocline allows us to simplify the problem and to study the inertial motions using a much simpler two-layer model. The predictions of the two-layer model are strongly supported by data. Because the time and space scales we deal with are small, longshore variations can be neglected.

In Sections 2 and 3 we present temperature and current data, and coherence computations showing strong baroclinic motions at frequencies close to the inertial frequency. The analytical linear model is developed in Section 4. In Section 5 we discuss the relationship between current and temperature in the inertial frequency band. In the Appendix B we estimate the frictional spin-down time due to bottom friction and conclude that it is much longer than the inertial period.

2. The site and the data

We shall discuss the temperature and current measurements obtained during different summers and at different places on the continental shelf (Fig. 1). The seasonal thermocline separates a bottom layer (minimum temperature value of ~13.5°C) from an upper layer with a mean temperature of ~20°C. The thermocline whose thickness is of the order of 10 m lies at about mid-depth (10–50 m) on the greater part of the shelf. Because of this peculiar feature, the gulf behaves like a two-layer fluid, at least in the inertial frequency band. This assumption is strongly supported by data analysis, as will be shown. Thus, a good representation of its dynamics is provided by two current measurements in the vertical, one in the surface layer, and one in the bottom layer, and temperature records over the whole depth. During the Port la Nouvelle experiment in 1975 (PN 75), the surface (bottom) current meter was set beneath a surface (subsurface) float, and the thermistor chain was supported by a two-leg mooring at a neighbouring location. During the LION 1977 (LI 77) and LION 1978 (LI 78) experiments, all measurements were made with a subsurface mooring (the thermistor chain was set between the current meters).[1] All the records were obtained within a band of 30′ in latitude (Fig. 1), and so the inertial period T_i was assumed to be constant at all the measurement points (T_i = 17 h 33 min at 43°N).

One of the major features emerging from the observations is that oscillations in the inertial frequency band in the current and temperature time series are generated by the onset of strong storm events (Fig. 2).

Typical stormy conditions are generally linked to the occurrence of a meteorological depression over

[1] The data collected in the "Golfe du Lion" during the three experiments are presented in internal reports of the Laboratoire d'Océanographie Physique du Muséum.

the Ligurian basin—the associated north-westerly winds, the Mistral and the Tramontane, rush through the passes dividing the Pyrenees, the Massif Central and the Alps, respectively. The wind speed increases and decreases very quickly, the direction is stable. Storms last from one to four days and occur about 10 times during one summer (Millot, 1979). Because of some instrumental failures, and for homogeneity between the different data sets, only selected records are considered during each experiment. All the time

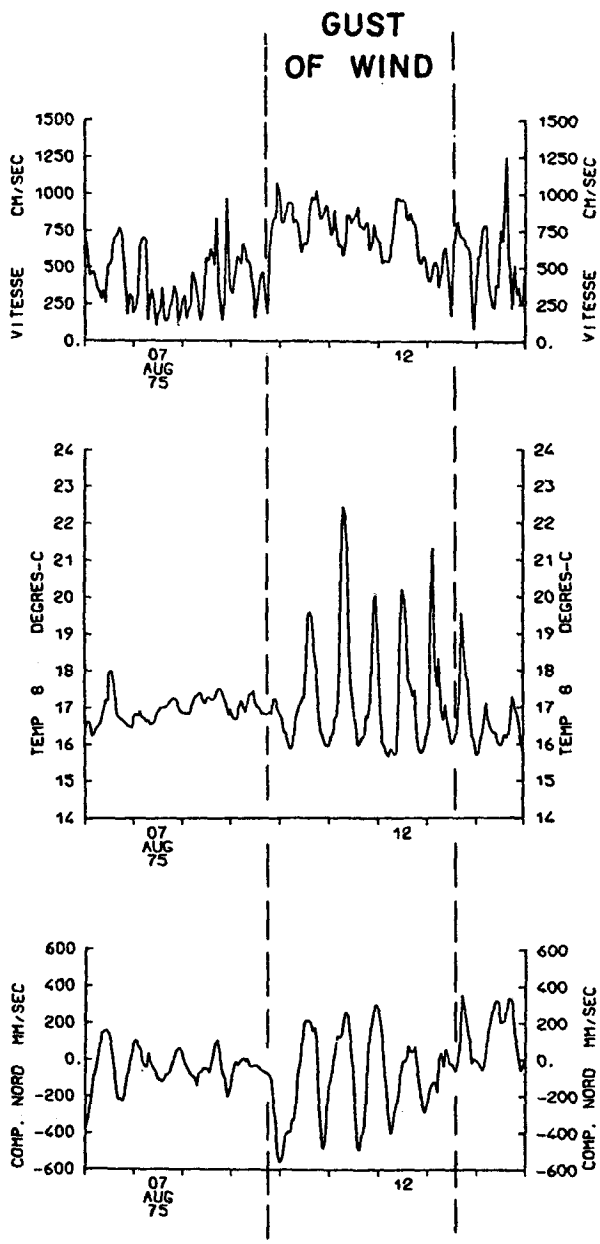

FIG. 2. The upper curve represents the wind speed measured in the vicinity of point 75 C (the dashed lines delimit a Tramontane event). The other records are obtained at 75 C. They show the sea temperature at 15 m and the north-south component of the current at 5 m. One clearly remarks that temperature and current oscillations are generated by the gust of wind of 9 August.

TABLE 1. Characteristics of the time series dealt with in the autospectral analysis.

Time series	Immersion of meter/ Bottom depth (m)	Length [hours = days (dates)]
Depth-averaged temperature		
75B*	0–20/25	2520 = 105 (19 Jun–2 Oct)
75C	15–50/55	1800 = 75 (19 Jun–2 Sept)
77B	16–51/65	1620 = 67.5 (2 Jul–7 Sept)
77C	15–50/91	2160 = 90 (2 Jul–30 Sept)
78A*	12–32/43	1980 = 82.5 (23 Jun–14 Sept)
78B	15–50/98	1980 = 82.5 (23 Jun–14 Sept)
78E	15–50/74	1980 = 82.5 (23 Jun–14 Sept)
Surface currents		
75B**	5/25	1710 = 71 (23 Jun–7 Oct)
75C**	5/55	1710 = 71 (19 Jun–7 Oct)
77B	10/65	1980 = 82.5 (2 Jul–22 Sept)
77C	10/91	2160 = 90 (2 Jul–30 Sept)
78A	10/43	1980 = 82.5 (23 Jun–14 Sept)
78B	10/98	1980 = 82.5 (23 Jun–14 Sept)
78E	10/74	1980 = 82.5 (23 Jun–14 Sept)
Bottom currents		
75B**	20/25	1710 = 71 (23 Jun–7 Oct)
75C	50/55	2640 = 110 (23 Jun–7 Oct)
77B	60/65	1980 = 82.5 (2 Jul–22 Sept)
77C	86/91	2160 = 90 (2 Jul–30 Sept)
78A	38/43	1980 = 82.5 (23 Jun–14 Sept)
78B	93/98	1980 = 82.5 (23 Jun–14 Sept)

* Only considered for coherence computations (depth < 50 m).
** Interrupted time series.

series obtained during the PN 75, LI 77, and LI 78 experiments are indicated in Table 1. Each time series lasted for two or three months, from late June or early July to late September. Recorders were Aanderaa current meters RCM-4 and thermistor chains TR-1; the sampling interval was 15 min for current and 30 min for temperature. Such sampling intervals can adequately resolve the inertial band.

The data were subjected to spectral analysis. The FFT (Hunt, 1975) was applied to time series 180 h in length. Spectral estimates were obtained at 25.7, 22.5, 20, 18, 16.4, 15, 13.8, 12.9 and 12 h with 18 to 24 degrees of freedom (d.f.).

a. Temperature measurements

The thermistor chains used have 11 equi-spaced (5 m) sensors; they were set from the surface to 50 m (PN 75), and from 15 to 65 m (LI 77 and LI 78). Down to about the 5 to 10 m depths, temperature records were influenced by the daily heating and cooling of the surface layers. At deeper locations, the main feature was the occurrence of temperature oscillations with frequencies close to the inertial frequency (f_i). Below 50 m, the temperature fluctuations were very small. Fig. 2 shows an example of the observed thermal features. We have often calculated thermocline displacements of 10 m. The records located near the thermocline level show sig-

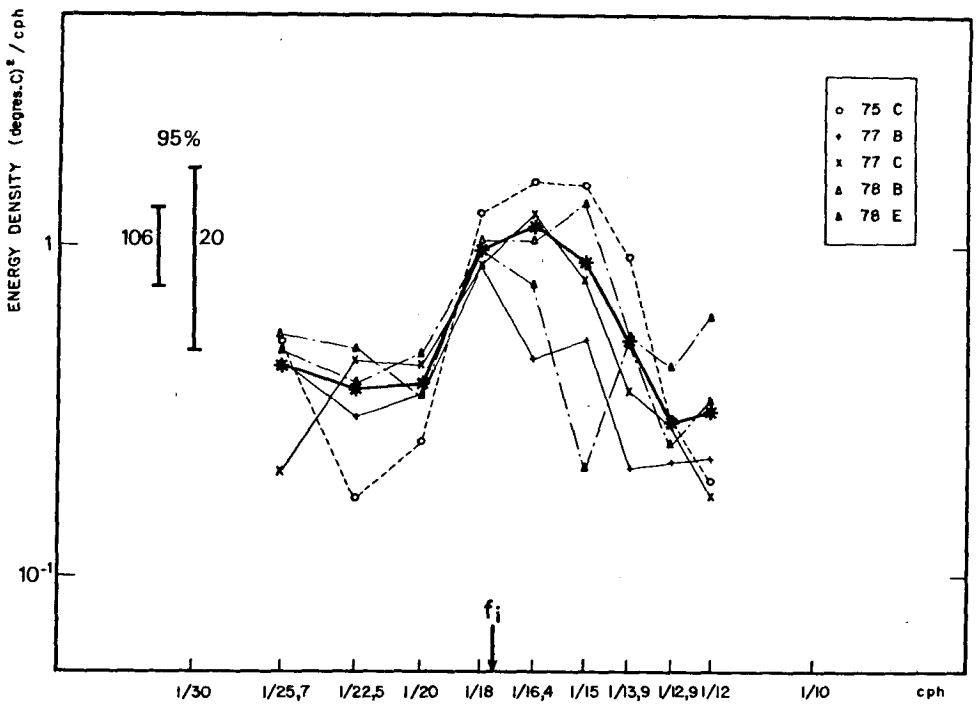

FIG. 3. Spectra of the depth-averaged temperatures (~20 d.f. each). The peak observed on the ensemble-averaged spectrum (full line, 106 d.f.) is centered on frequencies $> f_i$.

nals larger than those obtained in the bottom or surface layers; the mean depth of the thermocline is variable in time but the different records are still in phase in the inertial band.

In order to define the vertical displacements of the thermocline we computed a mean temperature profile within a depth interval including the thermocline level (eight measurements between 15 and 50 m). The spectral estimates of the five time series were plotted on a logarithmic scale (Fig. 3). In the studied frequency band, their values at different locations are very similar. This is rather unexpected when we consider the very different locations of the moorings with respect to the upwelling centers (Millot, 1979), and argues for some homogeneity between records obtained at different places and during different summers. The maximum energy densities (5–10 db above the continuum) are distributed over three adjacent frequency bands ($1/18$, $1/16.4$, $1/15$ cph). The 95% confidence interval with 20 d.f. is limited by factors of 0.48 and 1.71, and so the peak which occurs on each spectrum in the vicinity of f_i is significant.

To get the statistical behavior of the gulf, an ensemble-averaged spectrum (see Appendix A) representative of 53 pieces was obtained (Fig. 3) by summing the spectra computed at different locations and during different summers. As shown in Section 3, the depth-averaged temperature time series are noncoherent, thus the number of degrees of freedom of the ensemble-averaged spectrum is proportionally increased (95% bounds for 106 d.f. are 0.75 and 1.29). Energy densities at $1/18$, $1/16.4$, $1/15$ cph are of the same order and form a broad peak. The base of the peak (roughly defined by $1/20$ and $1/12.9$ cph), is centered on frequencies $> 1/16.4$ cph. These values are significantly different from f_i ($1/17.5$ cph); the relative difference between the periods is ~10%.

b. *Current measurements*

Surface current measurements were made at 5 m (10 m) below the surface during the PN 75 (LI 77 and LI 78) experiment. The deep current measurements were made at 5 m above the bottom at depths of 20 and 50 m (PN 75), 60 and 86 m (LI 77), 38 and 93 m (LI 78), (Table 1); these later records (except 75 B in late summer) were in the bottom layer.

Seven time series were obtained in the surface layer. On nearly all the clockwise spectra (Fig. 4a), the maximum energy density occurs at $-1/18$ cph and at $-1/16.4$ cph with slightly lower values. The peaks have differing amplitudes, but they are all centered in the vicinity of f_i. They are sharp and the energy densities at positive frequencies (Fig. 4b) are similar to each other. The ensemble-averaged spectrum of the seven time series also is presented in Fig. 4 (in full line). It gives an estimate of the dynamics of the gulf. As shown in Section 3, currents measured at two different locations are coherent at 95%, thus the number of degrees of freedom of the ensemble-averaged spectrum is increased linearly by summing spec-

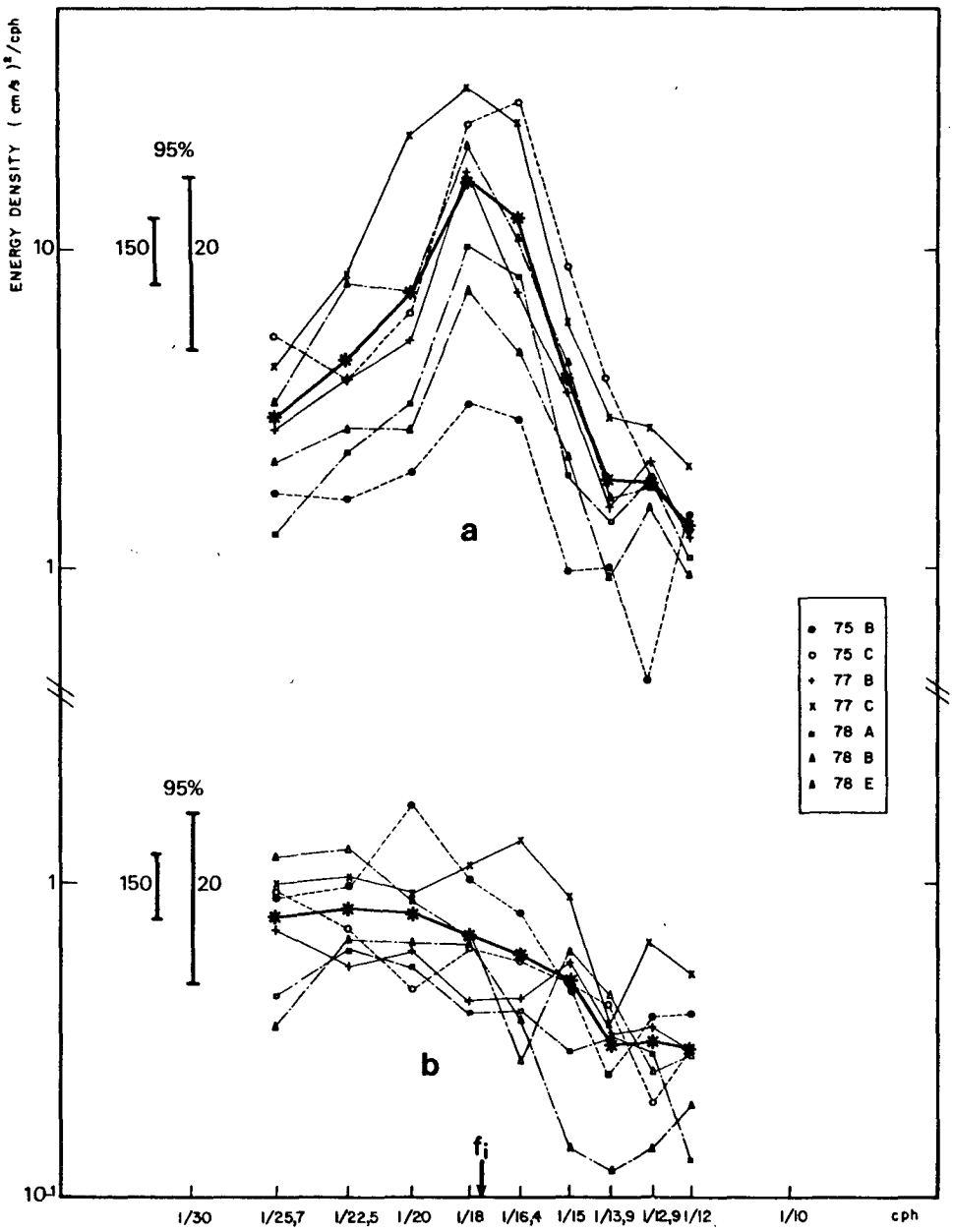

FIG. 4a. Clockwise spectra of the currents in the surface layer (~20 d.f. each). All the peaks are centered on f_i. The number of d.f. of the ensemble-averaged spectrum is <150.

FIG. 4b. Counterclockwise spectra. As expected, they are flat.

tra computed at different years but only slightly increased by summing spectra computed during the same year at different locations, which removes bias due to local effects. The top of the peak still occurs at $-1/18$ cph and at $-1/16.4$ cph.

The clockwise spectra obtained near the bottom (Fig. 5a) are less homogeneous than those obtained at the surface. The peak is not so well defined and its main frequency is much more variable. On four clockwise spectra out of six, the maximum energy is not observed at f_i and, moreover, all the peaks are centered on frequencies greater than f_i. The ensemble-averaged bottom autospectrum shows that the mean energy density level is ~10 db below the level of the surface one. The asymmetry of the peak of the ensemble-averaged spectrum suggests that it is centered on a frequency greater than f_i. All the ensemble-averaged spectra are drawn in Fig. 6.

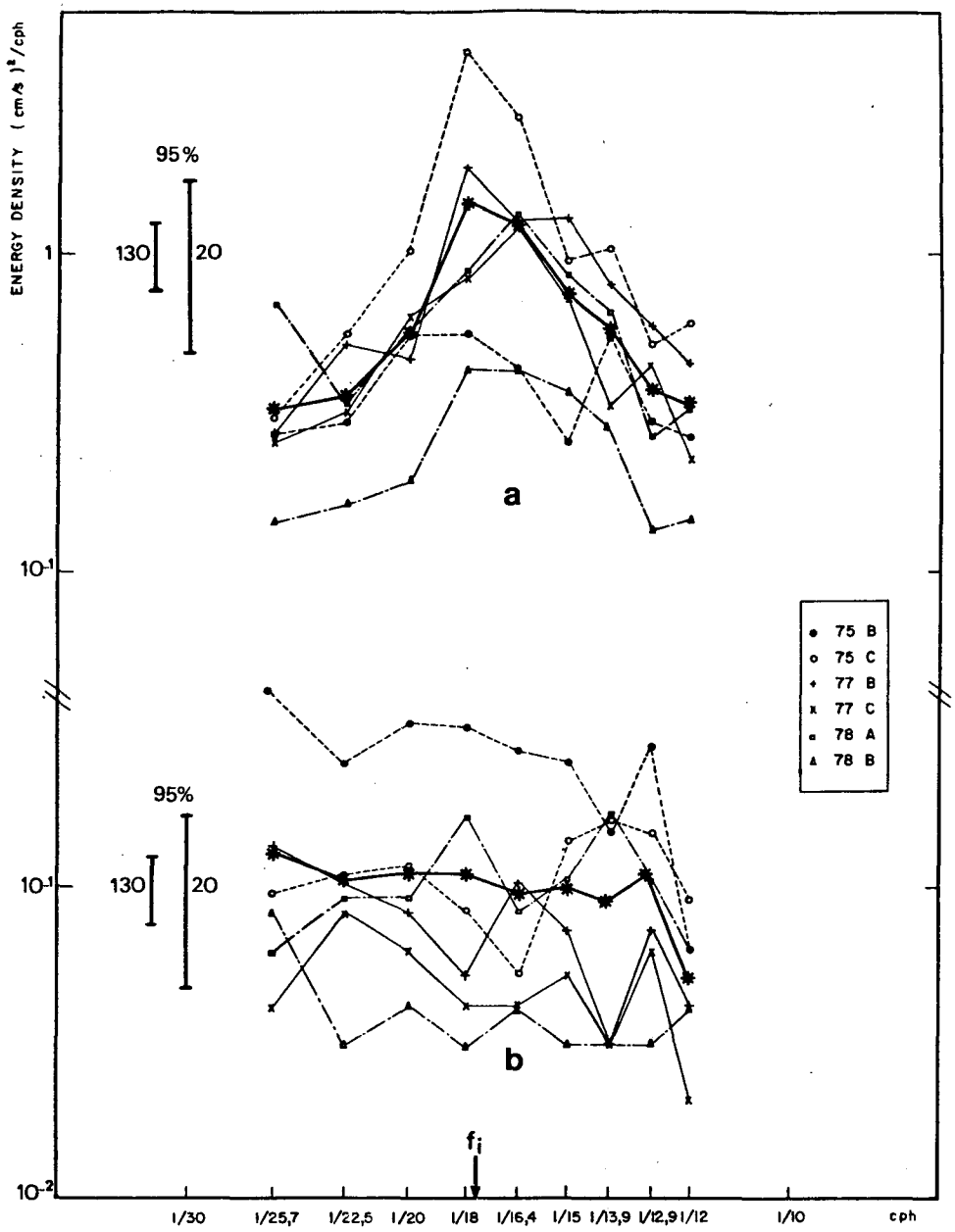

FIG. 5a. Clockwise spectra of the currents in the bottom layer (~20 d.f. each). Maximum energy densities on four of them occur at frequencies $> f_i$. This feature is emphasized by a flattening of the peak of the ensemble averaged spectrum (full line, <130 d.f.). 5b. As in Fig. 4b.

3. Coherence computations

Vectorial coherence is computed using the technique presented in Gonella (1972). In order to increase the stability of coherence, and thus to decrease the confidence limit, it is necessary to increase the number of d.f. of the estimates. Thus we deal with pieces of only 90 h duration each. Respectively, 19, 23 and 22 pieces are obtained for the 75, 77 and 78 experiments. The d.f. is ~40, and the 95% confidence limit is ~0.38. Coherence estimates are obtained in the inertial band at $1/22.5$, $1/18$, $1/15$, $1/12.9$ and $1/11.3$ cph.

a. Horizontal coherence in the surface layer

The distance between two simultaneous records ranged from 14 to 42 km (Table 2). Coherence and phase estimates computed for five pairs of vectors from $-1/11.3$ to $+1/11.3$ cph are displayed in Fig. 7. The maximum values of coherence (Fig. 7a) are reached

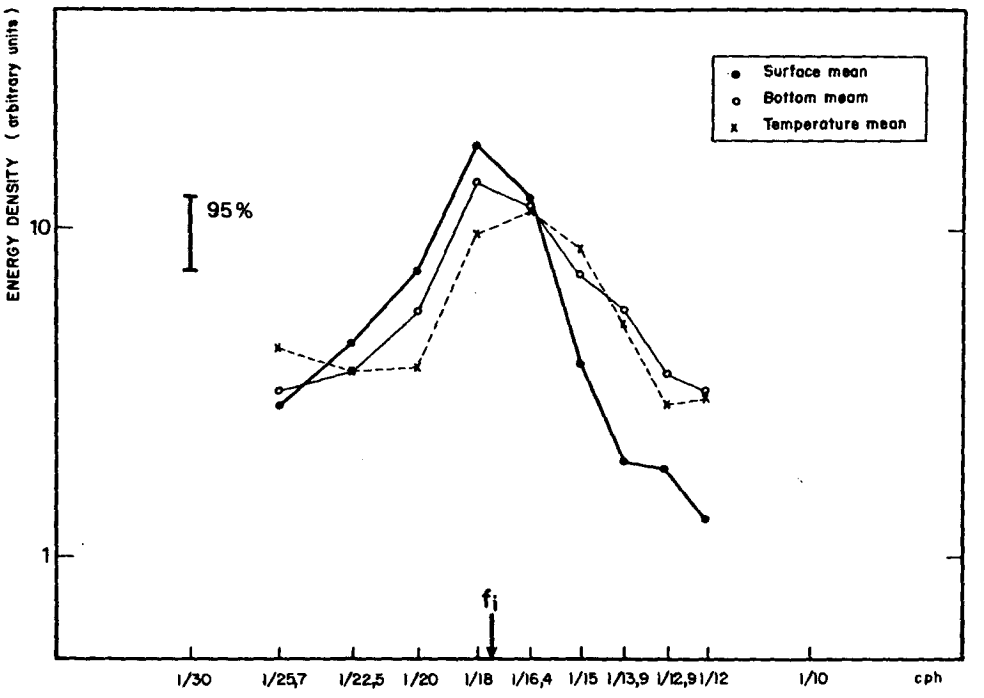

FIG. 6. The ensemble-averaged spectra of the depth-averaged temperatures and the clockwise currents in the surface and bottom layers (confidence interval for ~100 d.f.). The peak in the surface current spectrum is thinner and centered at f_i while the peaks in the bottom current and in the temperature spectra are centered at frequencies $> f_i$.

at negative frequencies between $-f_i$ and 0. In addition, one notes that the phases (Fig. 7b) in the inertial band are confined to a small interval around zero. Thus, the peaks in the velocity spectra at $-f_i$ (Fig. 4) correspond to highly coherent pure inertial waves oscillating in phase in the surface layer for each experiment. The relatively good coherence at the above frequencies is a common feature of the space variability of ocean currents (Gonella, 1972).

The coherence does not seem to depend on the distance between the moorings. Thus, an ensemble-averaged coherence has been computed (Appendix A), which is supposed to be representative of the dynamics of the surface layer (the phase lag is about zero). The ensemble-averaged coherence exceeds the 95% confidence level only at $-1/18$, $-1/22.5$ and $-1/30$ cph, and its values decrease as the frequency varies from $-f_i$ to 0.

TABLE 2. As in Table 1 except for coherence computations.

Coherences				
Currents		Depth-averaged temperatures separation (km)/length (h)	Depth-averaged temperature	
Surface layer/ separation (km)/length (h)	Vertical/ separation (m)/length (h)		Surface current/ length (h)	Bottom current/ length (h)
			Coastal points	
75B–75C/14/1710	75B/15/1710	75B–75C/14/1800	78A/1980	78A/1980
77B–77C/28/2070	75C/45/1710	77B–77C/28/1620	78E/1980	75C/1800
78A–78B/30/1980	77B/50/2070	78A–78B/30/1980	77B/1620	77B/1620
78A–78E/43/1980	77C/76/2070	78A–78E/43/1980	Offshore points	
78B–78E/30/1980	78A/28/1980	78B–78E/30/1980	77C/2160	77C/2160
	78B/83/1980		78B/1980	78B/1980

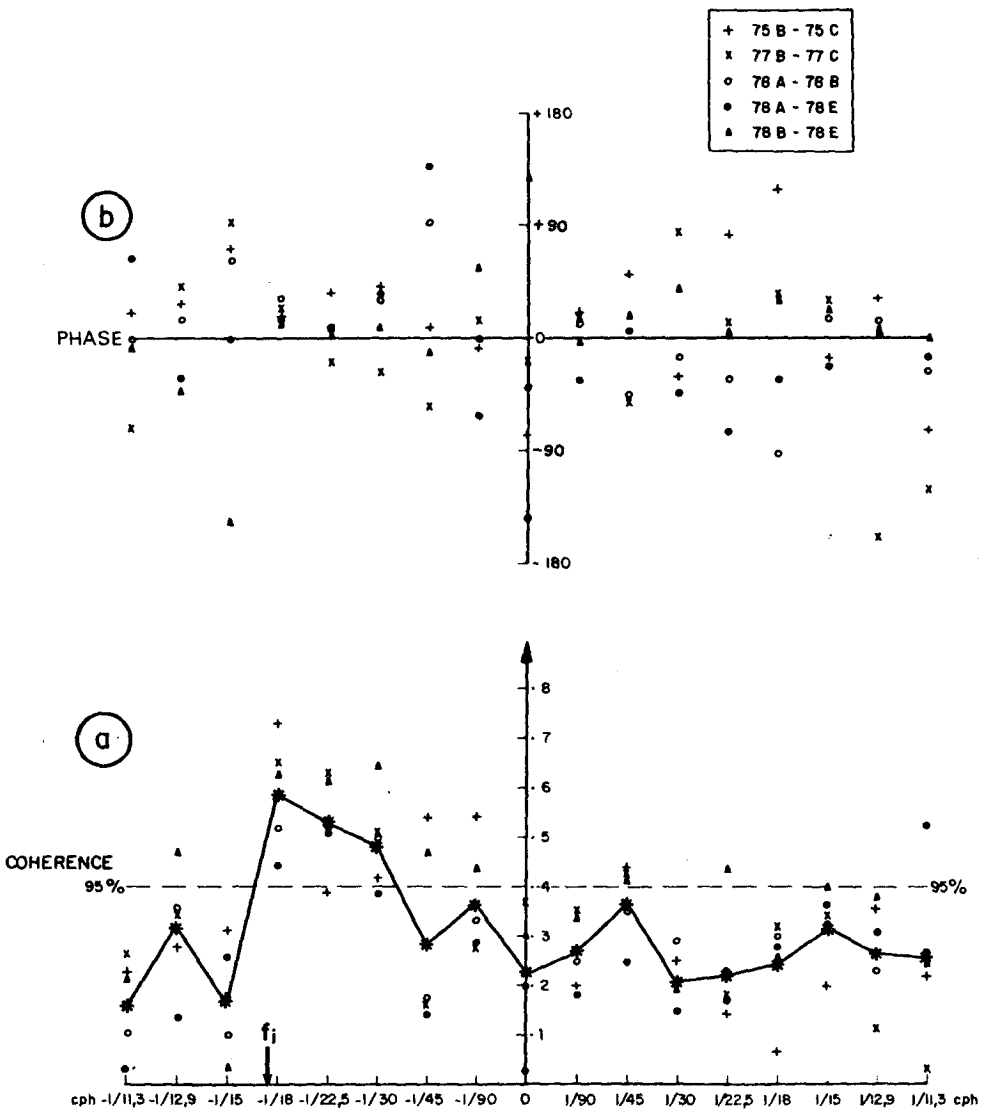

FIG. 7. The ensemble-averaged coherence in the surface layer (full line), is significant at 95% at f_i and the two adjacent lower frequencies only. The phases associated to high coherence values are approximately zero [with 40 d.f., the confidence interval at a coherence value of 0.5 (0.6) is ±25° (±20°)]. This is related to the slablike motion of the surface layer.

b. Coherence between currents in the surface and bottom layers at the same mooring

The vertical separation between the current meters ranged from 15 to 83 m. Fig. 8 displays the six-pair analysis. Maximum coherence is reached at $-1/18$, $-1/15$, $-1/12$ and $-1/11.3$ cph and phase lags of 180° are measured in the same band. As there is no clear dependence between the vertical distance and the coherence values, the ensemble-averaged coherence (in full line in Fig. 8) is supposed to be representative of the relations between the surface and bottom layers (the phase lag is 180°). Its maximum is obtained at $-1/15$ cph. All the estimates from $-1/18$ to $-1/11.3$ cph and beyond are significant at the 95% confidence level. The dashed curve shows the ensemble-averaged coherence estimates computed over 180 h pieces; the frequency of maximum coherence is still significantly different from f_i.

When isopycnals are horizontal, it is well known (Mooers, 1975; Phillips, 1977) that f_i is the lower bound of the internal gravity waves frequency band, a feature also predicted by the model (Section 4). So, a significant coherence in this frequency band is undoubtedly related to the occurrence of internal baroclinic waves. Let us emphasize that the frequency for which the coherence between the surface and bottom currents is maximum, coincides with the mean frequency of the peak of the temperature spectrum, and is different from the mean frequency

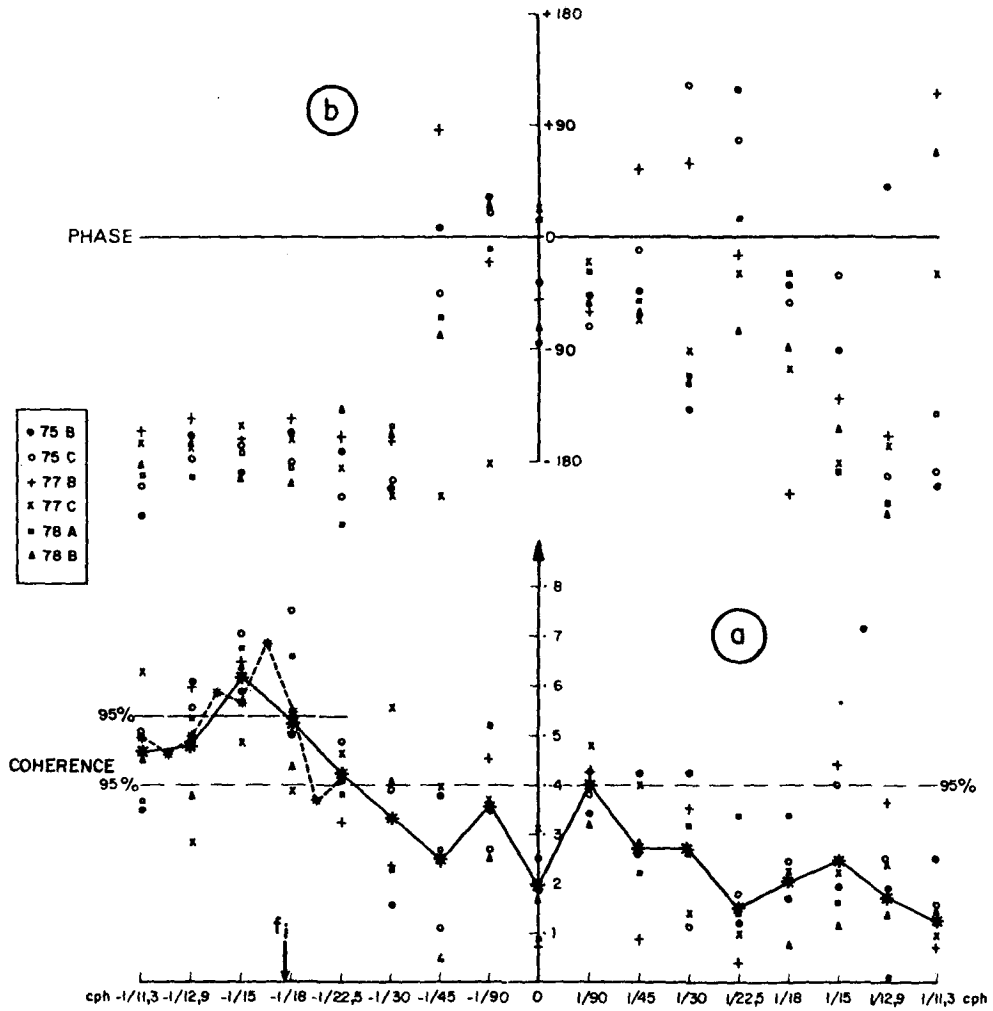

FIG. 8a. The ensemble-averaged coherence in the vertical (full line) is significant at 95% in the internal waves frequency band, from f_i beyond $-1/11$ cph. The maximum coherence is obtained at a frequency slightly $>f_i$ (the dashed curve is for pieces of 180 h in length).

FIG. 8b. When the coherence is large, the phase lag is π (as in Fig. 7b for the confidence limits).

of the peak of the current spectra (Fig. 6). The values of the coherence estimates at low frequencies ($-1/22.5$, $-1/30$ cph) are near the 95% confidence level and the associated phase lags are still about 180°. The phase lags of 180°, systematically observed between two points situated in each layer in a wide negative frequency band and whatever the vertical separation of the current meters is, strongly support the slablike motion of the two layers.

c. *Spatial coherence between the depth-averaged temperatures*

A significant coherence between the depth-averaged temperatures measured at different places was not found in the inertial band during the LION experiments. This feature is emphasized by the ensemble-averaged coherence in Fig. 9. This must be linked to the poor coherence observed in currents in the lower layer (not shown). The high value computed at $f = 0$ shows that the temperature variations induced by upwellings, advection or seasonal variability, occur on a large scale in the basin.

d. *Coherence between current and depth-averaged temperature at the same point*

In order to check the statistical-dependence between currents and depth-averaged temperature, a temperature vector was constructed. Its west-east component was equal to the depth-averaged temperature and its north-south component was set at zero. By comparison with a classical vector field decomposition (Gonella, 1972), this pseudo-vector

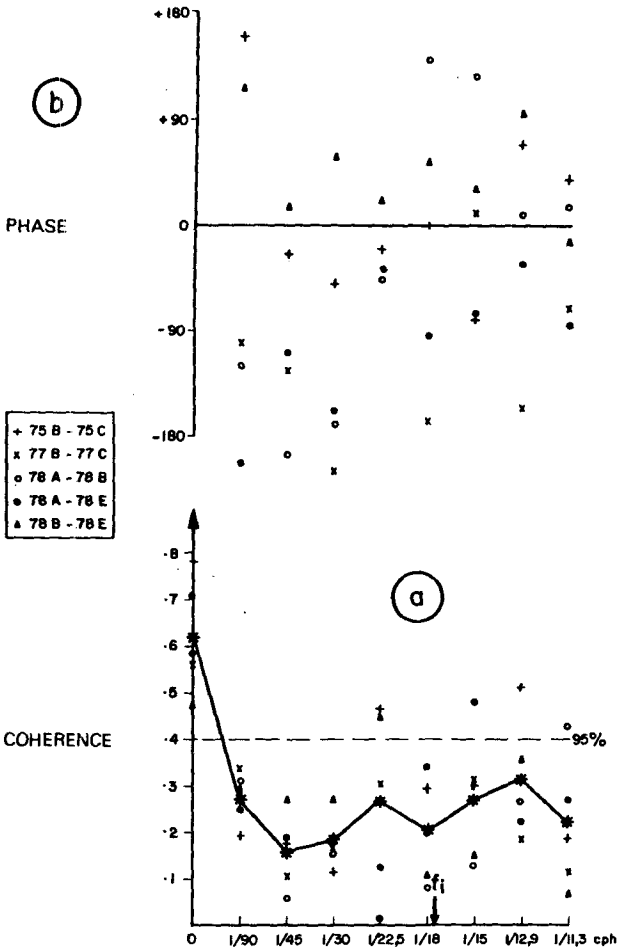

FIG. 9. The depth-averaged temperatures are non coherent spatially. Thus, the behavior of the internal waves are changing from one observation point to the other. High coherence at $f = 0$ indicates the occurrence of large-scale phenomena.

was decomposed into circularly polarized vectors of the same amplitude rotating clockwise and anticlockwise with the same angular velocity. Two classes of measurement-points are distinguished. At coastal points (located at <20 km offshore), the coherence is significant in the inertial band with a maximum at f_i; when the points are far from shore (>40 km), the coherence values are always lower than the 95% level of significance. The ensemble-averaged coherence in the negative frequency band is drawn for depth-averaged temperature and surface current, and for depth-averaged temperature and bottom current. At coastal points (Fig. 10), the coherence values are significant for frequencies in the band $-1/18$ to $-1/15$ cph for surface currents and down to $-1/13$ cph for bottom currents; the associated phase lags are nearly uniform for each pair (temperature-current) in a large frequency band. If the phase lag between temperature and surface current is φ, then the phase lag between temperature and bottom current is nearly $\varphi + 180°$. This is in agreement with the results of coherence between currents in the vertical. At offshore points (Fig. 11), the coherence values are not significant and the phases are very scattered. Note that even if the peaks in the depth-averaged temperature and bottom-current spectra are centered on frequencies significantly different from the inertial frequency, the maximum coherence occurs at this frequency.

4. Theory

Many observations can be explained by a transient two-layer model. We follow the method used by Crépon (1969).

a. Formulation

The density variation of the ocean is simplified by using a two-layer fluid. This is a crude, but realistic assumption corresponding to retention of only the first internal mode, which is the most important for small motions (Lightill, 1969; Gill and Clarke, 1974). Because of the small depths of the Gulf of Lions we will also investigate the effects of bottom friction on the motions.

Hydrostatic and Boussinesq assumptions are employed and we deal with the vertically averaged equations of hydrodynamics in each layer. Since we consider small perturbations from rest, the equations are linearized.

In the upper fluid

$$\frac{\partial}{\partial t}\mathbf{u}_1 + f\mathbf{z} \times \mathbf{u}_1 = -g\nabla\zeta_1 + \frac{1}{\rho_1 h_1}(\boldsymbol{\tau} - \boldsymbol{\tau}_I) \quad (4.1)$$

$$\frac{\partial}{\partial t}(\zeta_1 - \zeta_2) + \nabla h_1\mathbf{u}_1 = 0. \quad (4.2)$$

In the lower fluid

$$\frac{\partial}{\partial t}\mathbf{u}_2 + f\mathbf{z} \times \mathbf{u}_2$$

$$= -g\epsilon\nabla\zeta_2 - g(1-\epsilon)\nabla\zeta_1 + \frac{1}{\rho_2 h_2}(\boldsymbol{\tau}_I - \boldsymbol{\tau}_b), \quad (4.3)$$

$$\frac{\partial}{\partial t}\zeta_2 + \nabla h_2\mathbf{u}_2 = 0. \quad (4.4)$$

The terms are defined as follows:

ζ_1 (ζ_2)	elevation at sea surface (interface) from rest
$\mathbf{u}_1$ ($\mathbf{u}_2$)	averaged velocity in the upper fluid (lower fluid)
f	Coriolis parameter
g	acceleration of the gravity
ϵ	fractional change in density $[=(\rho_2 - \rho_1)/\rho_2]$
∇	two-dimensional operator $\partial/\partial x$, $\partial/\partial y$

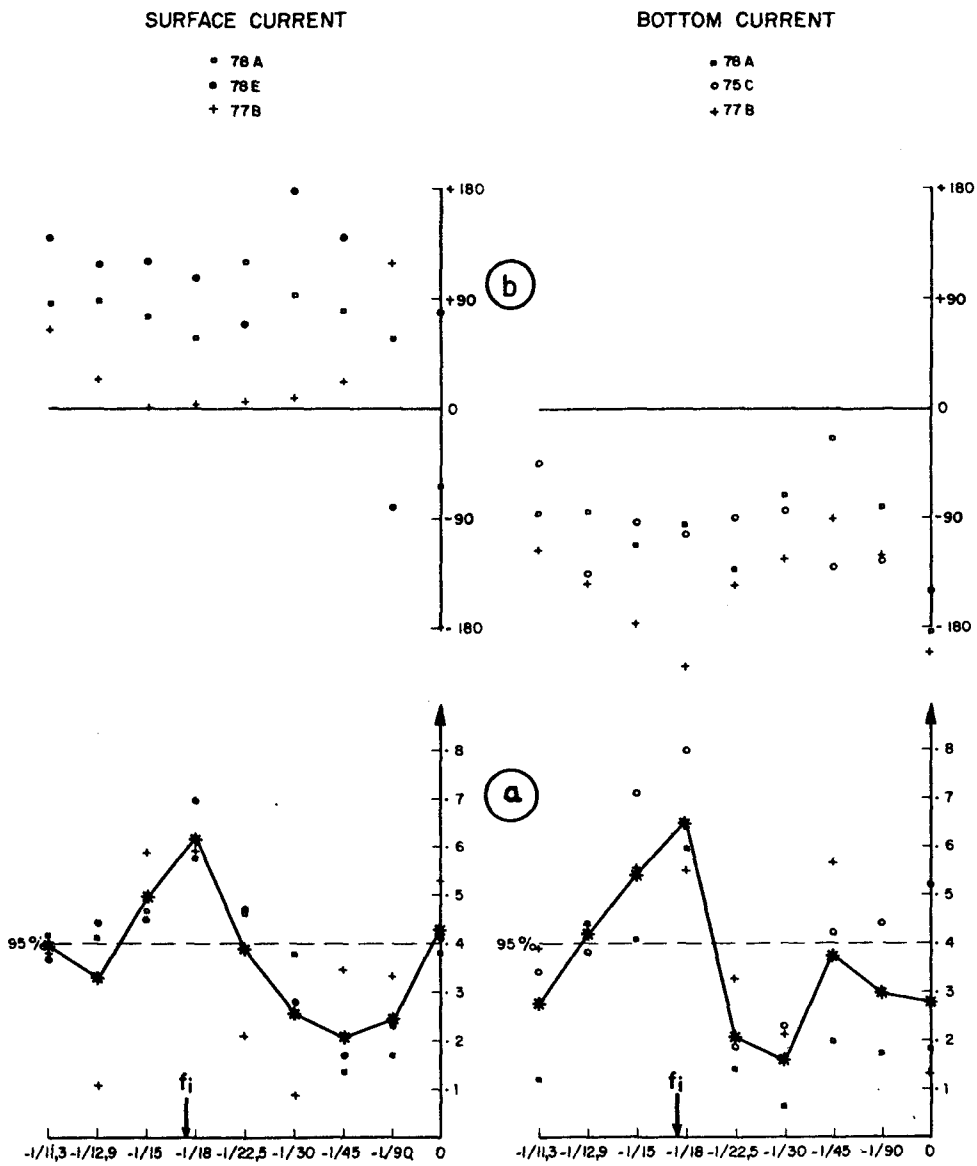

FIG. 10. At the coastal measurement points, coherences between the depth-averaged temperature pseudo-vector and currents in the two layers, are significant at frequencies $> f_i$, with maximum values at f_i. The phase lag of π is still observed in that figure.

$\mathbf{z}$	unit vector along the vertical axis, positive upward
h_1 (h_2)	thickness of the upper layer (lower layer) at rest
τ	stress at the sea surface
τ_I	stress at the interface
τ_b	bottom stress.

Because the time and space scales involved are small, we assume that f is constant as well as the total depth $h_1 + h_2 = H$.

Following Thompson and O'Brien (1973) we assume that τ_I is an order of magnitude less than τ_b and τ. Hence the coupling between the two layers is mainly due to pressure forces. The bottom stress is taken to be proportional to $\mathbf{u}_2$, i.e.,

$$\tau_b = \rho_2 h_2 \nu \mathbf{u}_2, \tag{4.5}$$

where ν, the damping coefficient, has the dimension of inverse time.

b. Method of solution

We study the motions generated along a straight coast, $x = 0$ (x oriented to the east and y to the north), by a transient atmospheric forcing. We assume that the parameters do not depend on y, i.e., $\partial/\partial y = 0$.

We apply a Laplace transform with respect to t:

$$Z_i(p, x) = \int_0^\infty e^{-pt}\zeta_i(t, x)dt = \mathcal{L}(\zeta_i),$$

$$\mathbf{U}_i(p, x) = \int_0^\infty e^{-pt}\mathbf{u}_i(t, x)dt = \mathcal{L}(\mathbf{u}_i),$$

$$\mathbf{T}(p, x) = \int_0^\infty e^{-pt}(\mathbf{x}\tau^x + \mathbf{y}\tau^y)dt = \mathcal{L}(\boldsymbol{\tau}).$$

From (4.1) and (4.3), $\mathbf{U}_i$ can be found in terms of Z_i; the substitution of these values into the Laplace transform of (4.2) and (4.4) gives

$$\frac{\partial^2}{\partial x^2} Z_1 - (p^2 + f^2)(Z_1 - Z_2)\frac{1}{gh_1} = \frac{1}{\rho_1 g h_1}\left(\nabla \mathbf{T} + \mathbf{z}\frac{f}{p}\nabla \times \mathbf{T}\right) \times (p + \nu)\frac{\partial^2}{\partial x^2}[(1 - \epsilon)Z_1 + \epsilon Z_2] - p[(p + \nu)^2 + f^2]Z_2\frac{1}{gh_2} = 0. \quad (4.6)$$

The solution of the homogeneous differential equation associated with (4.6) is of the form

$$Z = Ae^{\pm\alpha_i x},$$

where α_i is a positive eigenvalue of Eq. (4.6).

If $\boldsymbol{\tau}$ does not depend on x, and taking into account the radiation condition (the motions must vanish as x tends to infinity), the solution of (4.6) is

$$\left.\begin{aligned} Z_1 &= A_1 e^{-\alpha_1 x} + A_2 e^{-\alpha_2 x} \\ Z_2 &= B_1 e^{-\alpha_1 x} + B_2 e^{-\alpha_2 x} \end{aligned}\right\}, \quad (4.7)$$

where

$$B_i = \left(1 - \alpha_i^2\frac{gh_1}{p^2 + f^2}\right)A_i,$$

$$A_i = (-1)^i\frac{1}{\rho_1(gh_1)^2\epsilon}(fT^y + pT^x) \times \frac{p^2 + f^2 - \alpha_{3-i}{}^2 g\epsilon h_1}{(\alpha_1{}^2 - \alpha_2{}^2)p\alpha_i}.$$

Here A_i does not depend on x; it is determined by the boundary condition $\mathbf{u}_i(t, 0) = 0$.

c. Case where $\nu = 0$

This case has been abundantly studied in the literature; for a survey, see O'Brien *et al.* (1977).

We obtain the following values for α_i:

$$\alpha_1{}^2 = (p^2 + f^2)/c_1{}^2, \quad \alpha_2{}^2 = (p^2 + f^2)/c_2{}^2,$$

where $c_1 = (gH)^{1/2}$ is the speed of long barotropic waves, $c_2 = (g\epsilon h_1 h_2/H)^{1/2}$, the speed of long baroclinic waves.

When the wind is perpendicular to the shore, constant in space, and is a step function of time, of the form $\boldsymbol{\tau} = \tau_0 Y(t)\mathbf{x}$, we obtain

$$\left.\begin{aligned} \zeta_1 &= -\frac{\tau_0}{\rho_1 c_1 f}\left(\hat{\zeta}_1 + \frac{h_2 c_2}{h_1 c_1}\hat{\zeta}_2\right) \\ \zeta_2 &= -\frac{\tau_0}{\rho_1 c_1 f}\frac{h_2}{H}\left(\hat{\zeta}_1 - \frac{c_1}{c_2}\hat{\zeta}_2\right) \end{aligned}\right\}, \quad (4.8)$$

where

$$\left.\begin{aligned} \hat{\zeta}_i &= \mathcal{L}\left\{\frac{f}{p(p^2 + f^2)^{1/2}} \times \exp[-(p^2 + f^2)^{1/2}x/c_i]\right\} \\ \hat{\zeta}_i &= \int_0^{ft} J_0[f(t^2 - (x/c_i)^2)]Y(t - x/c_i)d(ft) \end{aligned}\right\}, \quad (4.9)$$

$Y(t)$ is the stepfunction, J_0 the Bessel function of first kind and zero order, and $\hat{\zeta}_i$ an elevation generated at the shore; its front propagates with the speed c_i.

The first oscillations of $\hat{\zeta}_i$ are shown in Fig. 12 and in Fig. 13. They have a period less than the inertial period, and the discrepancy grows with the offshore distance, as we can see in Table 3. This can explain the observations of Section 2 (Fig. 2), in particular, the fact that the most energetic parts of the depth-averaged temperature spectra are mainly located at frequencies $> f_i$.

As t tends toward infinity with x fixed, we obtain the asymptotic expansion of $\hat{\zeta}_i$ using the Sutton's algorithm (1934), which relates the large time behavior to algebraic expansions around the singularities of the Laplace transforms:

$$\hat{\zeta}_i \underset{t\to\infty}{=} e^{-x/r_i} + (2/\pi)^{1/2}(ft)^{-1/2}\sin(ft - \pi/4) + O[(ft)^{-3/2}], \quad (4.10)$$

where $r_i = c_i/f$, is the radius of deformation.

Because $c_1 \gg c_2$ the upwelling corresponds to the term $c_1/c_2\hat{\zeta}_2$ in the expression for ζ_2 in (4.8). From (4.10), we see that its spatial offshore scale is the internal radius of deformation c_2/f. The spin-up time T of $\hat{\zeta}_2$ (e-folding time) is given by the condition $(fT)^{3/2} = e$ which yields $T = \max(2f^{-1}, x/c_i)$.

The velocity $\mathbf{u}_1(t, x)$ in the upper fluid is given by

$$\mathbf{u}_1(t, x) = \mathbf{u}_L(t) - (h_1/H)\hat{\mathbf{u}}_1 - (h_2/H)\hat{\mathbf{u}}_2 \quad (4.11)$$

and in the lower fluid

$$\mathbf{u}_2(t, x) = -(h_1/H)(\hat{\mathbf{u}}_1 - \hat{\mathbf{u}}_2), \quad (4.12)$$

where $\mathbf{u}_L(t)$ is the velocity due to the local wind. This velocity is the velocity calculated by Pollard and

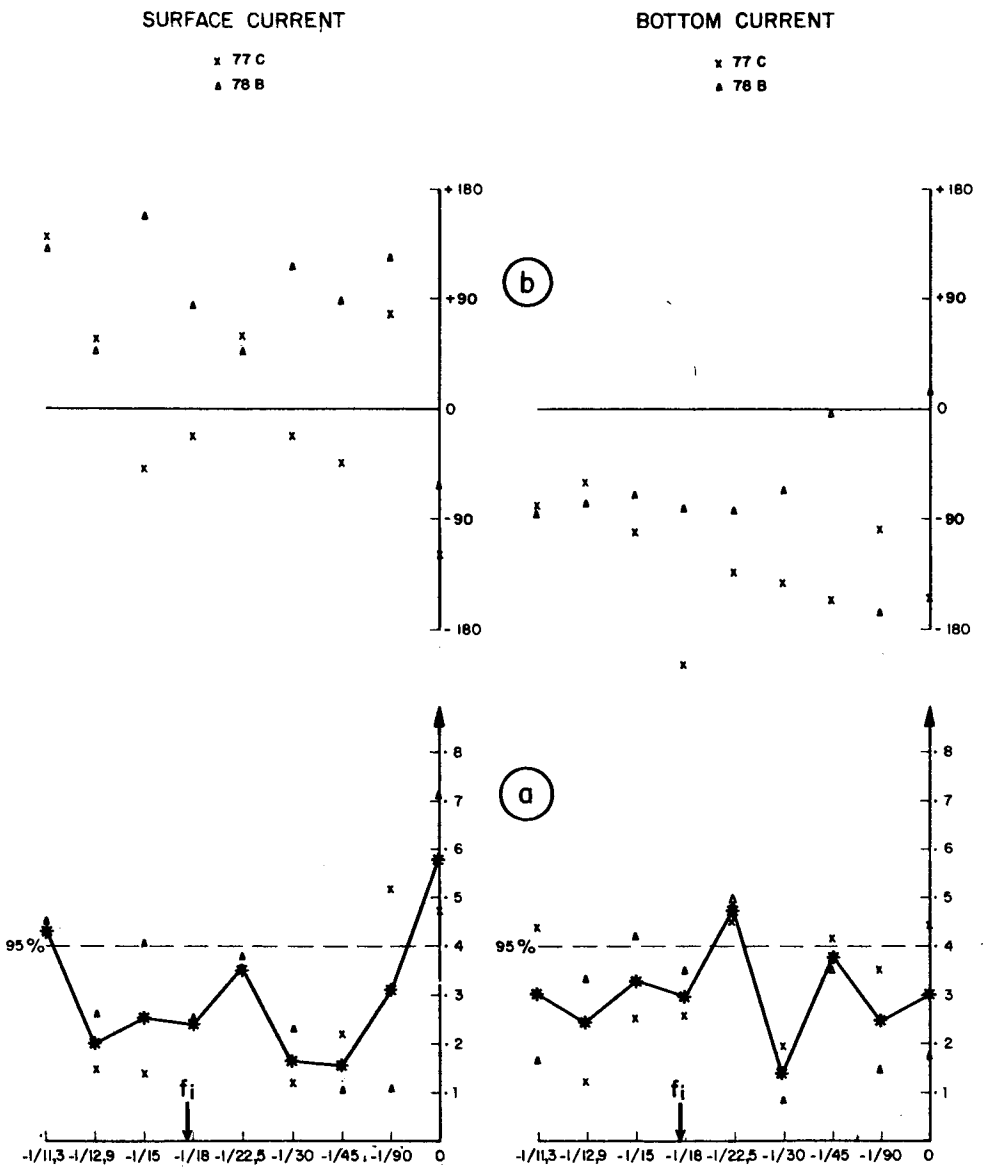

FIG. 11. Coherences at the offshore points are non-significant. Internal waves observed at these points come from different directions.

Millard (1970) in their simple, but realistic model of the dynamics of the upper ocean:

$$\mathbf{u}_L(t) = \frac{\tau_0}{\rho_1 h_1 f}\{\sin(ft)\mathbf{x} - [1 - \cos(ft)]\mathbf{y}\}Y(t). \quad (4.13)$$

Here $\hat{\mathbf{u}}_i$ is an elementary velocity generated at the shore in order to satisfy the boundary condition $u_i(t, 0) = 0$. Its front propagates with the speed c_i, i.e.,

$$\hat{\mathbf{u}}_i = \mathcal{L}\left\{\frac{\tau_0}{\rho_1 h_1}\frac{\exp[-(p^2 + f^2)x/c_i]}{p^2 + f^2} \times \left(\mathbf{x} - \frac{f}{p}\mathbf{y}\right)\right\}. \quad (4.14)$$

At $x = 0$, it is obvious from (4.14) and (4.11) that $\hat{\mathbf{u}}_i(t, 0) = \mathbf{u}_L(t)$. The velocity $\hat{\mathbf{u}}_i$ deforms as it propagates. Like $\hat{\zeta}_i$, $\hat{\mathbf{u}}_i$ is associated with a dispersive wave and its energy spreads out both in space and in time.

As $t \to \infty$, the asymptotic expansion of $\hat{\mathbf{u}}_i$ is

$$\hat{\mathbf{u}}_i \underset{t\to\infty}{=} \frac{\tau_0}{\rho_1 h_1 f}\{\sin(ft)\mathbf{x} - [e^{-x/r_i} - \cos(ft)]\mathbf{y} - (x/r_i) \times (ft)^{-1/2}(2/\pi)^{1/2}[\cos(ft - \pi/4)\mathbf{x} - \sin(ft - \pi/4)\mathbf{y}]\} + O[(ft)^{-3/2}]. \quad (4.15)$$

This asymptotic expansion is valid for $ft \gg x/r_i$.

The ratio c_2/c_1 is small. It is of the order of 2×10^{-2} on the continental shelf of the Gulf of Lions

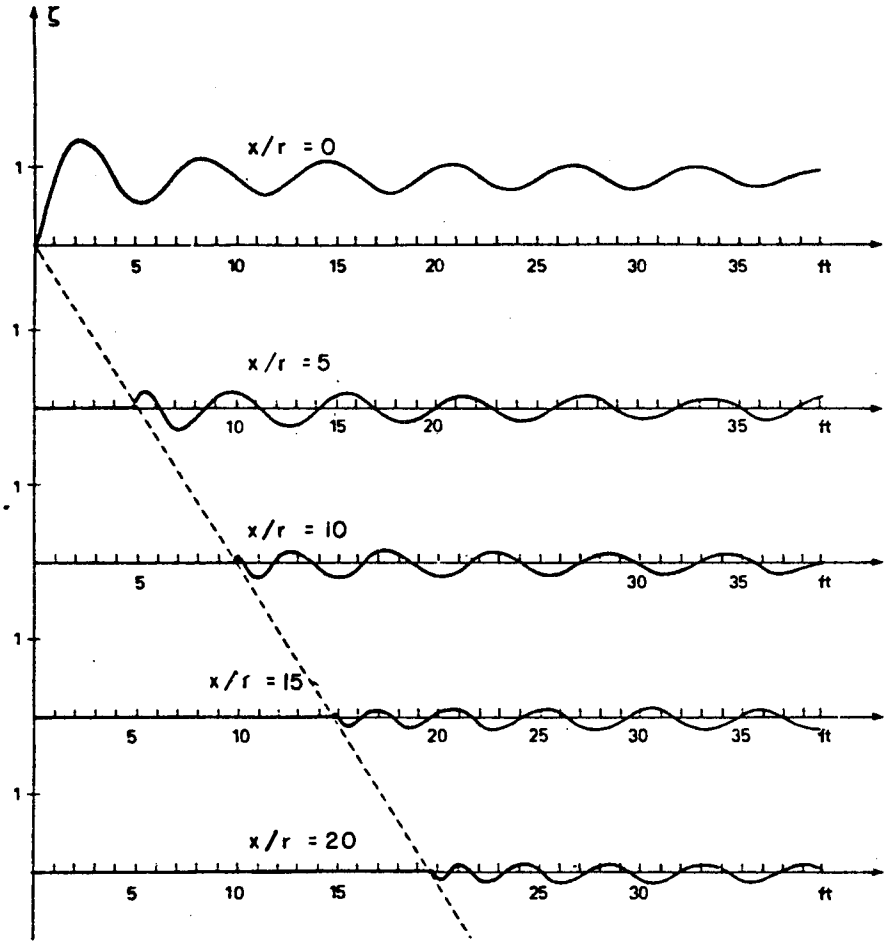

FIG. 12. Elevation at different distances from shore as a function of time.

($h_1 \approx h_2 \approx 20$ m; $\epsilon \approx 10^{-3}$; $c_1 \approx 20$ m s^{-1}; $c_2 \approx 0.5$ m s^{-1}; $r_1 \approx 200$ km; $r_2 \approx 5$ km). For $0 < x < r_2 \ll r_1$ and $ft > 2$, Eqs. (4.15) and (4.13) yield

$$\hat{\mathbf{u}}_1 = \mathbf{u}_L + O(c_2/c_1).$$

Hence, (4.11) and (4.12) can be written

$$\left.\begin{aligned} \mathbf{u}_1 &= \frac{\tau_0}{\rho_1 f H}\frac{h_2}{h_1}\{(e^{-x/r_2} - 1)\mathbf{y} + (x/r_2) \\ &\quad \times (ft)^{-1/2}(2/\pi)^{1/2}[\cos(ft - \pi/4)\mathbf{x} \\ &\quad - \sin(ft - \pi/4)\mathbf{y}]\} \\ \mathbf{u}_2 &= -\frac{h_1}{h_2}\mathbf{u}_1 \end{aligned}\right\} . \quad (4.16)$$

The spin-up time of (4.16) is $T = 2f^{-1}$. The inertial oscillations are polarized clockwise. The currents are baroclinic. The mean currents and the inertial oscillations in the upper and the lower layers have opposite phases, in agreement with the observations of Section 3.

When the wind is parallel to the shore and a step-function of time, the elevations ζ_1 and ζ_2 are given by (4.8) with $\hat{\zeta}_i$ replaced by $\hat{\zeta}_i'$, i.e.,

$$\hat{\zeta}_i' = \int_0^{ft} \hat{\zeta}_i d(ft). \quad (4.17)$$

The elevation $\hat{\zeta}_i'$ has the same properties as $\hat{\zeta}_i$, but its asymptotic expansion is different. One finds

$$\hat{\zeta}_i' \underset{t\to\infty}{=} e^{-x/r_i}(ft) - (2/\pi)^{1/2}(ft)^{-1/2} \times \cos(ft - \pi/4) + O[(ft)^{-3/2}]. \quad (4.18)$$

The upwelling is still driven by the second term on the right side in (4.8). The elevation increases linearly with time. From (4.18) we see that its spatial offshore scale is the internal radius of deformation, and its spin-up time is

$$T = \max(2f^{-1}, x/c_i).$$

The velocities in the upper and the lower fluids are given by (4.11) and (4.12) with $\mathbf{u}_L$ replaced by $\mathbf{u}_L'$,

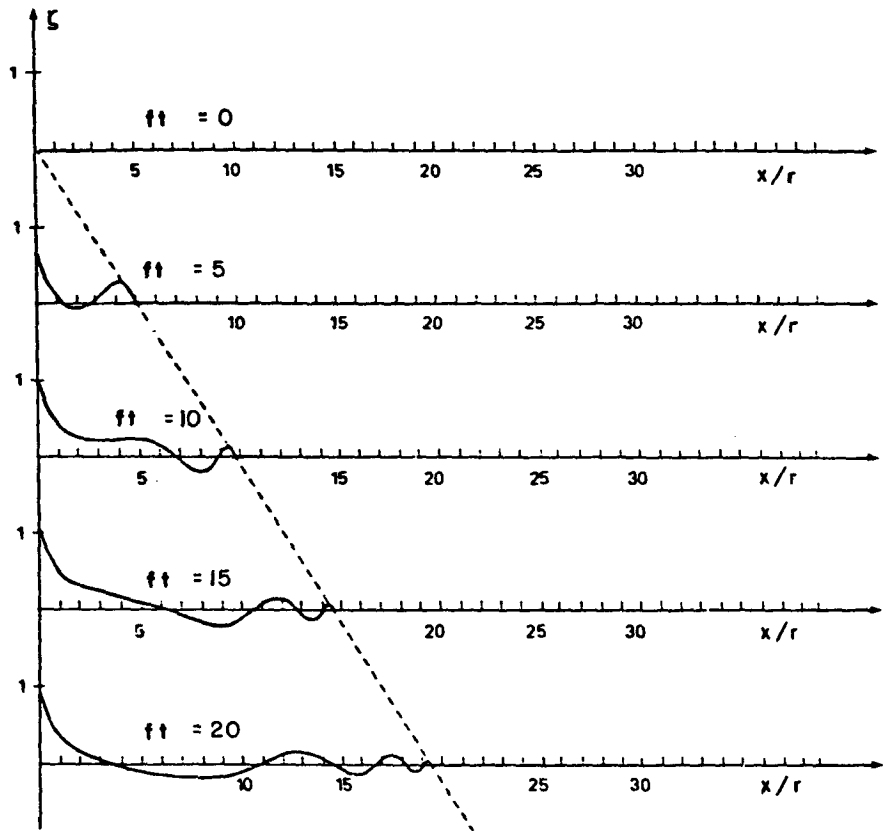

FIG. 13. Elevation at different times as a function of distance from shore.

$$\mathbf{u}_L'(t) = \mathbf{z} \times \mathbf{u}_L,$$

and $\hat{\mathbf{u}}_i$ by $\hat{\mathbf{u}}_i'$

$$\hat{\mathbf{u}}_i' = \mathcal{L}\left\{\frac{\tau_0}{\rho_1 h_1 f}\frac{f^2}{p(p^2+f^2)} \times \exp[-(p^2+f^2)^{1/2}x/c_i]\left(\mathbf{x} - \frac{f}{p}\mathbf{y}\right)\right\}.$$

Here $\hat{\mathbf{u}}_i'$ has properties similar to $\hat{\mathbf{u}}_i$, but its asymptotic expansion is different:

$$\hat{\mathbf{u}}_i' \underset{t\to\infty}{=} \frac{\tau_0}{\rho_1 h_1 f}\{[e^{-x/r_i} - \cos(ft)]\mathbf{x} - [e^{-x/r_i}(ft) - \sin(ft)]\mathbf{y} - (x/r_i)(ft)^{-1/2}(2/\pi)^{1/2} \times [\sin(ft - \pi/4)\mathbf{x} + \cos(ft - \pi/4)\mathbf{y}]\} + O[(ft)^{-3/2}]. \quad (4.19)$$

This asymptotic expression is valid for $ft \gg x/c_i$.

In the ocean, $h_1 \ll H$ and for $0 < x < r_2 \ll r_1$ the most important velocities are given by the first and the third term of (4.11). Taking into account (4.19), $\mathbf{u}_1$ is

$$\mathbf{u}_1 = \frac{\tau_0}{\rho_1 h_1 f}[e^{-x/r_2}(ft)\mathbf{y} + (1 - e^{-x/r_2})\mathbf{x}] + O[x/r_2(ft)^{-1/2}].$$

Thus in that case there is generation in the upper layer of a coastal boundary jet parallel to the shore of a width of the order of c_2/f, which was described by Charney (1955), Csanady (1977). The e-folding time T is given by (4.19):

$$T = \max[10(x/r_2)^2 f^{-1}, x/c_i].$$

For continental shelf processes, for the same values of parameters defined above, and if $0 < x < r_2 \ll r_1$ and $ft > x/r_2$, Eqs. (4.11), (4.12) and (4.19)

TABLE 3. Ratio of the first periods (T) of the oscillations of the elevation with respect to the inertial period (T_i) at different offshore distances (x/r) for a wind perpendicular to the shore. We emphasize the spatial and temporal variability of the ratio T/T_i.

$x/r = 0$	$x/r = 5$	$x/r = 10$
0.995	0.708	0.468
0.999	0.915	0.755
0.999	0.962	0.872

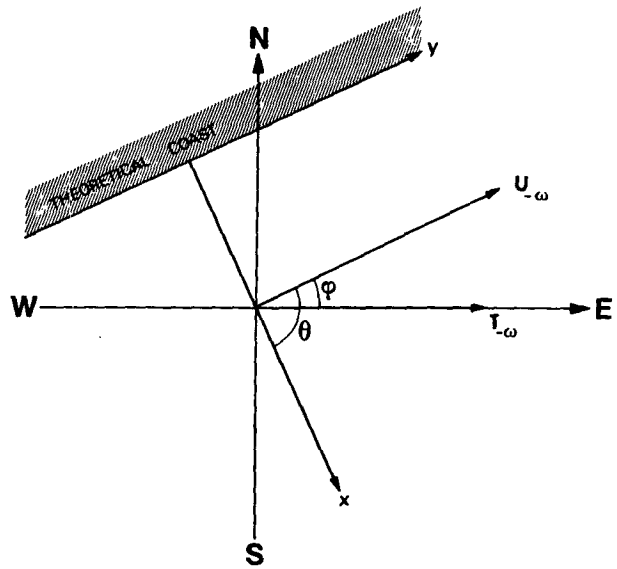

FIG. 14. The phase lag φ at $-f_i$ computed from coherence analysis between the temperature pseudo-vector and the current. When the Fourier component of the temperature at $-f_i$ is maximum, the clockwise component of the temperature pseudo vector T_{-f_i} is to the east ($T_{u_{f_i}} = T_{-f_i} + T_{+f_i}$). Thus, φ is the angle of the current parallel to the shore, and $\theta = \varphi - \pi/2$ is the direction of propagation of the internal waves.

yield

$$\left.\begin{aligned}\mathbf{u}_1 = \frac{\tau_0}{\rho_1 Hf}\frac{h_2}{h_1}\Big\{\Big(\frac{h_1}{h_2} + e^{-x/r_2}\Big)fty \\ + (1 - e^{-x/r_2})\mathbf{x} + (x/r_2)(ft)^{-1/2} \\ \times (2/\pi)^{1/2}[\sin(ft - \pi/4)\mathbf{x} \\ + \cos(ft - \pi/4)\mathbf{y}]\Big\}\end{aligned}\right\}, \quad (4.20)$$

$$\left.\begin{aligned}\mathbf{u}_2 = \frac{\tau_0}{\rho_1 Hf}\{(1 - e^{-x/r_2})(fty - \mathbf{x}) \\ - (x/r_2)(ft)^{-1/2}(2/\pi)^{1/2} \\ \times [\sin(ft - \pi/4)\mathbf{x} + \cos(ft - \pi/4)\mathbf{y}]\}\end{aligned}\right\}$$

where the spin-up time of (4.20) is $T = 2f^{-1}$.

On the continental shelf, the behavior of currents is similar to that in (4.16). The inertial oscillations are polarized clockwise. The mean current perpendicular to the shore and the inertial oscillations are in opposite phases in the two layers, but the mean current parallel to the shore increases linearly with time and has a tendency to become semi-barotropic for distances off the shore of the order of r_2. This agrees with the observations of currents off the Oregon shore where the wind is parallel to a straight coastline (Smith, 1974).

The case where $\nu \neq 0$, is studied in Appendix B. The behavior is quite similar to the case $\nu = 0$ at short times ($t < 10f^{-1}$) and an increase of the internal radius of deformation is found at large times.

5. Further comparisons between theory and observation

In Sections 2 and 3 we have mentioned the observed features which are explained by the theory presented in Section 4. Another very important result concerns relations existing between current, thermocline level, and direction of propagation of the internal waves. When the thermocline oscillations reach a maximum or a minimum value, the model of Section 4 predicts that the inertial component of the current is parallel to the coast, as can be seen in (4.10) and (4.16) or in (4.17) and (4.19). This is a consequence of the generation of baroclinic modes at the shore. Thus, according to this remark, it is possible to calculate the orientation of the coast or equivalently the direction of propagation of the baroclinic modes. (This direction is perpendicular to the shore.)

Our aim is to compare the computed and actual mean coastal orientations in order to support the above theory of coastal generation of the internal waves in the inertial frequency band.

We now consider the complex Fourier development of a time series

$$F(t) = \sum_{n=-\infty}^{+\infty} F_n e^{j\omega t}, \quad F_n = L^{-1}\int_0^L F(t)e^{-j\omega t}dt.$$

F_n and F_{-n} are complex conjugated ($F_{\pm n} = Fe^{\pm j\beta_n}$) when $F(t)$ is a scalar, and are independent when $F(t)$ is the complex number associated to a vector time series. Let 0° denote the eastward direction (Fig. 14). Coherence analysis between two time series $T(t)$ and $\mathbf{u}(t)$ gives the phase-lags $\varphi_{\pm n}$ between $T_{\pm n}$ and $u_{\pm n}$ which are the vectors associated to the frequencies $\omega_{\pm n} = \pm n/L$. For a scalar time series like the mean temperature $T(t)$, the signal at the frequencies ω_n is

$$Te^{j\beta_n}e^{j\omega_n t} + Te^{-j\beta_n}e^{-j\omega_{-n}t} = 2T\cos(\omega_n t + \beta_n).$$

This signal is largest when $\omega_n t + \beta_n = 0$ and the clockwise and counterclockwise vectors are directed eastward. Therefore, the angle found at the inertial frequency on coherence between the current and the mean temperature vector is the angle of the current parallel to the shore and the west-east axis. The currents obtained when the depth-averaged temperature is maximum and the direction of propagation of the internal waves is at a right angle are shown in Fig. 14. The directions drawn in Fig. 15 are computed with surface and bottom measured currents. Taking into account the great complexity of natural conditions, and the restrictive approxi-

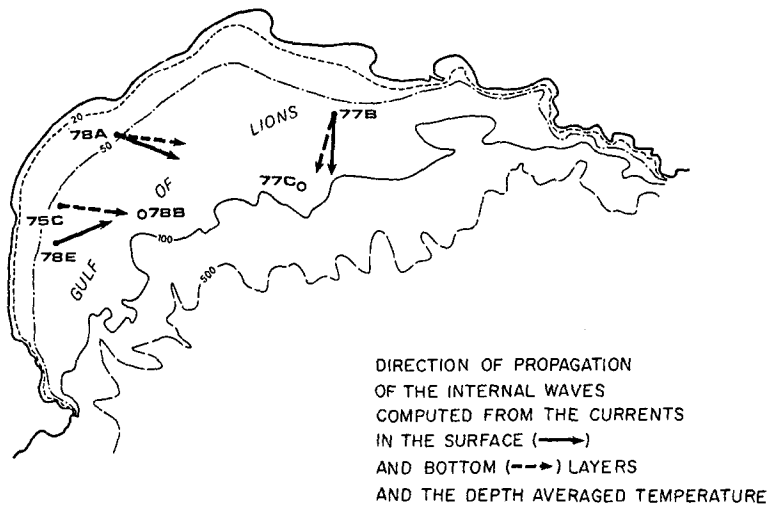

FIG. 15. Direction of propagation of the internal waves at f_i were obtained from coherence computations between the depth-averaged temperature and the currents. The relationship with the nearest coastal zone is noteworthy and argues for a coastal generation of the internal waves.

mations of the theoretical solutions (only valid for large t), the result is clearly noteworthy. The computed direction of propagation always corresponds to waves propagating from the nearest shore-located source of the internal wave field (i.e., the most influential source). Let us emphasize that the poor coherence between mean temperature and currents at the offshore points is due to the fact that no single coastal source is dominant; in that case, a local elevation of the thermocline is associated with variable current directions and thus, with variable directions of propagation.

6. Discussion

The observations that have been presented are deduced from many and long time series, and are statistically significant. They are obtained in a region where the tidal influence is very small, and then the response of the ocean-to-meteorological forcing can be studied without any bias. We have found many points of agreement between the observed dynamics of the Gulf of Lions in the inertial frequency band and the two-layer linear model presented in Section 4.

Inertial oscillations which are a common feature of deep-sea motions are observed there both on current and temperature records near the shore in summer. Their generation is due to transient gusts of wind of a duration of a few days (the Mistral and the Tramontane). The phenomena are well reproduced by the model.

Spectra of current time series in the surface layer show a thin peak at the inertial frequency f_i. This is explained by (4.11) which shows that the inertial oscillations in the upper layer are strongly dependent on the local wind.

The peaks on the spectra of the bottom currents and the depth-averaged temperatures are broader and centered on frequencies greater than f_i. This is due to the existence of long gravity waves of frequency greater than f_i generated at the shore, which drive the interface elevation [baroclinic wave Eq. (4.8)] and the bottom current [barotropic and baroclinic waves (4.12)]. We remark that the bottom current does not depend on the local wind forcing.

Coherence analysis shows that currents in the surface layer are in phase at frequencies $\leq f_i$. This must still be related to the local wind forcing of the currents in the upper layer [Eq. (4.11)], whose space scale is larger than the distance between the moorings, and whose time scale is of a few days. The bottom currents and the depth-averaged temperature measured at different moorings are noncoherent because they are associated to long dispersive waves.

At the same mooring, surface and bottom currents are coherent in a large band of frequencies $\geq f_i$, with a phase-lag of π. This is explained by Eq. (4.6) which is valid a few hours after the onset of the wind. Let us emphasize that this phase-lag of π, obtained whatever the separation in depth of the current meters is, shows that the internal waves occur on the first baroclinic mode only, and strongly supports the validity of the two-layer model and the slablike motion in each layer.

Currents and the depth-averaged temperature pseudo-vector measured at the same mooring, are coherent at f_i when the mooring is located at distances from shore less than 20 km; these parameters

are noncoherent at larger distances. When the coherence is significant, the direction of propagation of the internal waves can be computed; this direction is in agreement with their generation at the shore. The non-significant coherence obtained at moorings far from shore can be explained by the different coastal sources of internal waves, as is expected for moorings located near the center of a semicircular gulf.

The strong stratification observed in summer and the small depth of the basin make it possible to represent the Gulf of Lions by a two-layer fluid. The ratio of the vertical scale (depth) over the horizontal scale (internal radius of deformation) is $< 10^{-2}$, which enhances the validity of the shallow water hypothesis and the slablike motion in each layer.

In fact, the dynamics of the Gulf of Lions is associated to the transient phase of a geostrophic adjustment process due to the meteorological forcing, which generates long barotropic and baroclinic gravity waves at the shore. The variations of the depth-averaged temperature are modeled by the elevation of the interface which corresponds to the oscillations of the long baroclinic gravity waves. The current in the bottom layer is associated to the barotropic and baroclinic gravity waves while the current in the surface layer mainly depends on the local forcing.

Acknowledgments. This research was supported by the Centre National pour l'Exploitation des Océans and by the Centre National de la Recherche Scientifique. Data processing has been performed at the "Centre d'Essais de la Méditerranée" in Toulon. We are grateful to Dr. C. Winant for stimulating discussions, and we thank Dr. A. Lamy and Miss M. Heulot for their help in processing the data.

APPENDIX A

Degrees of Freedom of Spectral Analysis

We use p_n to denote the number of degrees of freedom of the spectrum $E_n(\omega)$ or of the coherence $C_n(\omega)$. The ensemble-averaged spectrum is obtained by

$$\bar{E}(\omega) = \frac{\sum_n p_n E_n(\omega)}{\sum_n p_n}.$$

If the time series are not coherent, the number of degrees of freedom of $\bar{E}(\omega)$ is $\sum_n p_n$ and so its confidence limit interval is smaller than any elementary confidence limit interval. If we apply the same operator to coherence, we obtain an ensemble averaged coherence $\bar{C}(\omega)$ whose curve is smoother than any single curve, but its confidence limit interval remains the same (if the p_n are of the same order of magnitude).

APPENDIX B

Analytical Results in the Case $\nu \neq 0$

In the case where $\nu \neq 0$, we obtain

$$\alpha_1^2 = \frac{K^2}{gh_2} \frac{p^2 + f^2}{p^2 + f^2 + K^2 h_1/h_2},$$

$$\alpha_2^2 = \frac{1}{g\epsilon h_1}(p^2 + f^2 + K^2 h_1/h_2),$$

where

$$K^2 = \frac{p}{p + \nu}((p + \nu)^2 + f^2).$$

Using (4.7) and the Laplace inversion formula, one can show that ζ_i is the sum of two elevations generated at the shore, whose fronts still propagate with the velocities c_1 and c_2 defined above.

The elevations ζ_1 and ζ_2 are difficult to calculate. Nevertheless, we can obtain their asymptotic expansions as t tends toward infinity using Sutton's algorithm (1934). We focus our attention on the case in which the wind is parallel to the shore because the elevations are much larger. Assuming that $\epsilon < \nu/f \ll 1$, we then obtain

$$\left.\begin{aligned}
\zeta_1 \underset{t\to\infty}{=} & -\frac{\tau_0}{\rho_1 c_1' \nu}\left\{2\left(\frac{\nu t}{\pi}\right)^{1/2} - \frac{xf}{c_1'} + \frac{c_2'}{c_1'}\left[\frac{h_2}{h_1}(\nu t) - \frac{1}{2}\left(3 + \frac{fx}{c_2'}\right)\right]e^{-fx/c_2'}\right. \\
& \left. - \left(\frac{\nu}{f}\right)^{3/2}\left(\frac{2}{\pi}\frac{h_2}{h_1}\right)^{1/2}(\nu t)^{-1/2}\cos(ft - \pi/4)\right\} + O[(\nu t)^{-1/2}], \\
\zeta_2 \underset{t\to\infty}{=} & -\frac{\tau_0}{\rho_1 c_1' \nu}\left(2\left(\frac{\nu t}{\pi}\right)^{1/2} - \frac{xf}{c_1'} - \frac{c_1'}{c_2'}\left[\left[\nu t - \frac{1}{2}\frac{h_1}{h_2}\left(1 + \frac{fx}{c_2'}\right)\right]e^{-fx/c_2'}\right.\right. \\
& \left.\left. + \left(\frac{\nu}{f}\right)^{3/2}\left(\frac{2}{\pi}\frac{h_2}{H}\right)^{1/2}(\nu t)^{-1/2}e^{-\nu_1 t}\cos(ft - \pi/4)\right]\right) + O[(\nu t)^{-1/2}]
\end{aligned}\right\}, \quad (4.21)$$

where $c_1' = (gh_2)^{1/2}$, $c_2' = (gh_1\epsilon)^{1/2}$, and ν_1 is the real part of the complex conjugated roots or the equation $\alpha_2^2 = 0$ (ν_1 is positive and $\nu_1 < \nu$).

Comparison of (4.18) and (4.21) leads to the following remarks. The bottom stress modifies completely the barotropic motion. The barotropic term of elevation grows like $(\nu t)^{1/2}$ instead of ft when $\nu = 0$. The baroclinic term keeps the same form, but the internal radius of deformation which is now $(g\epsilon h_1)^{1/2}/f$, is increased (by a factor 1.4 in the Gulf of Lions). The upwelling is still driven by the baroclinic term of ζ_2 (term multiplying c_1'/c_2'), and its magnitude at the shore is nearly identical to that obtained in (4.18).

Its spin-up time T' is of the order $T' = 10\nu^{-1}$. The ratio ν/f is small. As it is shown below, $\nu/f < 10^{-1}$. The spin-up time T of the upwelling without damping, is at least fifty times smaller than $T'(T/T' = 0.2\nu/f)$. Thus, at small times ($ft < 10$) the upwelling behaves like (4.8), and as the time increases ($\nu t > 10$), it behaves like (4.21).

The asymptotic values of the components of the velocities parallel to the shore are

$$\left.\begin{aligned} v_1 &= \frac{\tau_0}{\rho_1 h_2 \nu}\left[1 - \exp(-xf/c_2') + \left(\frac{h_2}{h_1}\nu t - \frac{xf}{2c_2'}\right)\exp(-xf/c_2')\right] \\ v_2 &= \frac{\tau_0}{\rho_1 h_2 \nu}[1 - \exp(-xf/c_2')]. \end{aligned}\right\} \quad (4.22)$$

We still observe a boundary coastal jet in the upper layer and its magnitude at the shore is similar to that obtained in (4.20) when $t \to \infty$. We also observe a tendency of the velocity to barotropy as the offshore distance increases.

From the above considerations we can conclude that a linear bottom stress slightly modifies the behavior of the upwelling and that the results of the case $\nu = 0$ are valid to a good accuracy for short times ($\nu t < 1$).

Remark

We estimate ν in the following manner. The bottom stress is equal to (Thompson and O'Brien, 1973)

$$\tau_b = \rho c |\mathbf{u}_2| \mathbf{u}_2, \quad (4.23)$$

where $c = 10^{-3}$.

Comparing (4.23) and the value of τ_b given in (4.5), we find

$$\nu = c|\mathbf{u}_2|/h_2.$$

An order of magnitude of $|\mathbf{u}_2|$ is 0.2 m s^{-1}, and for 20 m $< h_2 <$ 80 m, we find 2×10^{-6} s$^{-1} < \nu < 10^{-5}$ s^{-1}.

REFERENCES

Blanton, J. O., 1975: Nearshore lake currents measured during upwelling and downwelling on the thermocline in Lake Ontario. *J. Phys. Oceanogr.*, **5**, 111–124.

Blumen, W., 1972: Geostrophic adjustment. *Rev. Geophys. Space Phys.*, **10**, 485–528.

Charney, J. G., 1955: The generation of oceanic currents by winds. *J. Mar. Res.*, **14**, 477–498.

Crépon, M., 1969: Hydrodynamique marine en régime impulsionnel. *Cah. Océanogr.*, **21**, 863–877.

Csanady, G. T., 1977: The coastal jet conceptual model in the dynamics of shallow seas. *The Sea*, Vol. 6, E. D. Goldberg, Ed., Wiley, 117–144.

Gill, A. E., and A. J. Clarke, 1974: Wind-induced upwelling, coastal currents and sea level changes. *Deep-Sea Res.*, **21**, 325–345.

Gonella, J., 1971: A local study of inertial oscillations in the upper layers of the ocean. *Deep-Sea Res.*, **18**, 775–788.

——, 1972: A rotary-component method for analysing meteorological and oceanographic vector time series. *Deep-Sea Res.*, **19**, 833–846.

Hayes, S. P., and D. Halpern, 1976: Observations of internal waves and coastal upwelling off the Oregon coast. *J. Mar. Res.*, **34**, 247–267.

Hunt, M., 1975: TIMSAN analysis program. Internal report, Woods Hole Oceanographic Institution, Woods Hole, Mass.

Ivanov, Y. A., and Y. G. Morozov, 1977: A study of current velocity and temperature oscillations with periods close to the inertial period. *Izv. Atmos. Ocean. Phys.*, **13**, 125–129.

Lightill, M. J., 1969: Dynamic response of the Indian Ocean to the onset of the southwest monsoon. *Phil. Trans. Roy. Soc. London*, **A265**, 45–92.

Malone, F. D., 1968: An analysis of current measurements in Lake Michigan. *J. Geophys. Res.*, **73**, 7065–7081.

Millot, C., 1979: Wind induced upwellings in the Gulf of Lions. *Oceanol. Acta*, **2**, 262–274.

Mooers, C. N. K., 1975: Several effects of a baroclinic current on the cross-stream propagation of inertial internal waves. *Geophys. Fluids Dyn.*, **6**, 245–275.

Mortimer, C. H., 1977: Internal waves observed in Lake Ontario during IFYGL 1972. Descriptive survey and preliminary interpretation of near-inertial oscillations in terms of linear channel-wave models. Great Lakes Research Division, Spec. Rep. No. 32, 122 pp.

O'Brien, J. J., *et al.*, 1977: Upwelling in the ocean: Two and three-dimensional models of upper ocean dynamics and variability. *Modelling and Prediction of the Upper Layers of the Ocean*, E. B. Kraus, Ed., Pergamon Press, 178–228.

Phillips, O. M., 1977: *The Dynamics of the Upper Ocean*, 2nd ed. Cambridge University Press, 336 pp.

Pollard, R. T., 1970: On the generation by winds of inertial waves in the ocean. *Deep-Sea Res.*, **17**, 795–812.

——, and R. C. Millard, 1970: Comparison between observed and simulated wind-generated inertial oscillations. *Deep-Sea Res.*, **17**, 813–821.

Smith, R. L., 1974: A description of current, wind and sea level variations during coastal upwelling off the Oregon coast, July–August 1972. *J. Geophys. Res.*, **79**, 435–443.

Sutton, W. G., 1934: The asymptotic expansion of a function whose operational equivalent is known. *J. London Math. Soc.*, **9**, 131–137.

Thompson, J. D., and J. J. O'Brien, 1973: Time-dependent coastal upwelling. *J. Phys. Oceanogr.*, **3**, 33–46.

Verber, J. L., 1964: The detection of rotary currents and internal waves in Lake Michigan. Great Lakes Res. Div., Publ. No. 11, 382–389.

——, 1966: Inertial currents in the Great Lakes. Great Lakes Res. Div., Publ. No. 15, 375–379.

Webster, F., 1968: Observation of inertial period motions in the deep sea. *Rev. Geophys.*, **6**, 473–490.